IVYSPRING INTERNATIONAL PUBLISHER

Theranostics

2018; 8(16): 4491-4508. doi: 10.7150/thno.26291

Research Paper

Therapeutic mesopore construction on 2D Nb_2C MXenes for targeted and enhanced chemo-photothermal cancer therapy in NIR-II biowindow

Xiaoxia Han[1], Xiangxiang Jing[2]✉, Dayan Yang[2], Han Lin[3], Zhigang Wang[1], Haitao Ran[1], Pan Li[1]✉ and Yu Chen[3]✉

1. Chongqing Key Laboratory of Ultrasound Molecular Imaging, Ultrasound Department of the Second Affiliated Hospital of Chongqing Medical University. Chongqing, 400010, P. R. China.
2. Department of Ultrasound, Hainan General Hospital, Haikou, 570311, P. R. China.
3. State Key Laboratory of High Performance Ceramics and Superfine Microstructure, Shanghai Institute of Ceramics, Chinese Academy of Sciences, Shanghai, 200050, P. R. China.

✉ Corresponding authors: cqlipan@163.com (P. Li); ljjxx2000@126.com (X. Jing); chenyu@mail.sic.ac.cn (Y. Chen)

Received: 2018.03.26; Accepted: 2018.07.15; Published: 2018.08.07

Abstract

Two-dimensional (2D) MXenes have emerged as a promising planar theranostic nanoplatform for versatile biomedical applications; but their *in vivo* behavior and performance has been severely influenced and hindered by a lack of necessary surface chemistry for adequate surface engineering. To solve this critical issue, this work employs versatile sol-gel chemistry for the construction of a unique "therapeutic mesopore" layer onto the surface of 2D niobium carbide (Nb_2C) MXene.

Methods: The *in situ* self-assembled mesopore-making agent (cetanecyltrimethylammonium chloride, in this case) was kept within the mesopores for efficient chemotherapy. The abundant surface saline chemistry of mesoporous silica-coated Nb_2C MXene was further adopted for stepwise surface engineering including PEGylation and conjugation with cyclic arginine-glycine-aspartic pentapeptide c(RGDyC) for targeted tumor accumulation.

Results: 2D Nb_2C MXenes were chosen based on their photothermal conversion capability (28.6%) in the near infrared (NIR)-II biowindow (1064 nm) for enhanced photothermal hyperthermia. Systematic *in vitro* and *in vivo* assessments demonstrate targeted and enhanced chemotherapy and photothermal hyperthermia of cancer (U87 cancer cell line and corresponding tumor xenograft; inhibition efficiency: 92.37%) in the NIR-II biowindow by these mesopore-coated 2D Nb_2C MXenes.

Conclusion: This work not only significantly broadens the biomedical applications of 2D Nb_2C MXene for enhanced cancer therapy, but also provides an efficient strategy for surface engineering of 2D MXenes to satisfy versatile application requirements.

Key words: MXene, mesoporous silica, enhanced therapy, nanomedicine, cancer

Introduction

Based on their unique physiochemical properties and abundant compositions/nanostructures, two-dimensional (2D) materials have emerged as one of the most explored materials for versatile applications [1-3]. It is well known that the nanoparticles (NPs) or their composites are the crucial factors determining the performance and clinical translation potential of theranostic nanomedicines [4-10]. The fast development of 2D nanoscience has significantly promoted the biomedical applications of 2D nanoplatforms in theranostic nanomedicine [11-18]. Their unique physiochemical properties

endow these nanosheets with specific responses to external triggers, such as the well-established photo-responsive photothermal therapy (PTT) and photodynamic therapy (PDT) [19-21]. In addition, their structural features can be used for the construction of versatile vectors for the delivery of therapeutic agents [22-24].

Recently, 2D MXenes, as novel functional planar materials, have attracted broad attention from the scientific community because of their large number of family members and corresponding unique physiochemical properties [25-34]. In particularly, we and other researchers recently demonstrated that 2D MXenes such as titanium carbide (Ti_3C_2) and niobium carbide (Nb_2C) MXenes can be used for photo-triggered cancer hyperthermia based on their high photothermal conversion capability [35-39]. In addition, the unique composition of tantalum carbide (Ta_3C_4) MXene (Ta element has a high atomic number) has been developed for contrast-enhanced computed tomography (CT) of tumors [40]. Additionally, the high biocompatibility and biosafety of Ti_3C_2, Nb_2C and Ta_3C_4 MXenes have been preliminarily demonstrated, showing strong potential for further clinical translation [36, 37, 40]. Although these preliminary biomedical application results are promising, there still exists a big challenge for improving the theranostic performance of these 2D MXenes. Especially, the absence of desirable surface chemistry makes it highly challenging to control the surface status and surface engineering of these 2D nanosheets, which is of great significance for practical *in vivo* applications. For instance, targeted transportation of 2D MXenes into the tumor could guarantee high therapeutic efficacy, but targeted surface engineering and other surface-specific multifunctionalizations (*e.g.*, enhanced therapeutic functionality) still encounter significant challenges that must be addressed.

In this work, we report the construction of "therapeutic mesopores" onto the surface of 2D niobium carbide (Nb_2C) MXenes to solve two critical issues in the surface engineering and multifunctionalization of 2D MXenes. Their synthesis is based on typical sol-gel chemistry, which achieved a uniform therapeutic mesoporous-silica shell coating on the surface of Nb_2C MXenes. In particularly, the mesopore-making agent was *in situ* kept within the mesopores for chemotherapeutic purposes, for which no additional chemotherapeutic drugs were required. The other importance of this mesopore construction on 2D Nb_2C MXene is reflected by further stepwise surface PEGylation and targeted conjugation of cyclic arginine-glycine-aspartic pentapeptide c(RGDyC) (as the targeting peptide), which achieved targeted accumulation of these MXene composite nanoplatforms in tumor tissue and corresponding high enhanced therapeutic efficacy. The strategy of "therapeutic mesopores" construction on 2D MXenes provides an efficient strategy for broadening the biomedical applications of 2D MXenes, which takes the unique features of mesoporous structures as the reservoir for loading/delivery of therapeutic agents, abundant silica chemistry for surface engineering, and the high photothermal conversion performance of 2D MXenes. 2D Nb_2C MXenes were chosen in this work based on their photothermal conversion capability in the near-infrared (NIR)-II biowindow (1000-1350 nm) [41-42], which has much higher tissue-penetrating capability than widely explored light in the NIR-I biowindow (750-1000 nm); but, photothermal conversion nanoagents in the NIR-II biowindow have rarely been developed and reported.

Methods

Synthesis of 2D Nb_2C MXene nanosheets

Nb_2AlC powder (10 g, Forsman Scientific Co., Ltd, Beijing, China) was added to hydrofluoric acid (60 mL, 50% HF, Sinopharm Chemical Reagents Co., Ltd., Shanghai, China) aqueous solution under stirring for 48 h at room temperature to remove the middle Al layer in the crystal. After centrifugation and washing with ethanol and water three times to remove residual HF, the collection was immersed into tetrapropylammonium hydroxide (TPAOH, 50 mL, 25 wt%, J&K Scientific Co., Ltd., Beijing, China) aqueous solution and stirred for 3 d at room temperature. Finally, the Nb_2C MXene nanosheets were collected after washing by ethanol and water three times and re-dispersed in ethanol at 4 °C for storage.

Synthesis of Nb_2C-MSN and CTAC@Nb_2C-MSN composite nanosheets

Cetanecyltrimethylammonium chloride (CTAC, 1.0 g, Sigma-Aldrich Co., Ltd., Shanghai, China) was pre-mixed with water (5 mL) to prepare surfactant solution. Then, triethanolamine (TEA, 0.01 g, Sinopharm Chemical Reagents) was diluted by water at a ratio of 1:10 and subsequently added into the pre-arranged CTAC aqueous solution under stirring for 20 min at room temperature. Nb_2C aqueous solution (10 mL, 0.5 mg/mL) was dispersed into the above mixture by magnetic stirring and ultrasound treatment. Then, tetraethylorthosilicate (TEOS, Sinopharm Chemical Reagents, 100 μL) was added to the system dropwise and the reaction was kept at 80 °C in a water bath. Finally, the product was collected by centrifugation and washed by ethanol and water to remove impurities. The prepared CTAC@Nb_2C-MSN

composite nanosheets were stored at 4 °C for further use. To produce Nb_2C-MSN composite nanosheets, CTAC was extracted by hydrochloric acid (HCl)-diluted ethanol solution (1:10 in volume) three times at 78 °C.

Surface PEGylation and targeted RGD modification

To obtain amino-modified CTAC@Nb_2C-MSN, triethoxysilane (APTES, 100 μL, Sigma-Aldrich) was added to the CTAC@Nb_2C-MSN ethanol solution (100 mL), which was then stirred at 80 °C for 8 h. After washing, the amino-modified CTAC@Nb_2C-MSN was re-dispersed into phosphate buffered saline (PBS, 25 mL). NHS-PEG2000-MAL (100 mg, Sigma-Aldrich Co., Ltd., Shanghai) was added into the solution and the reaction was kept for 24 h at room temperature. After further washing and re-dispersion in PBS, cyclic arginine-glycine-aspartic pentapeptide c(RGDyC) (50 mg, CL Biochem, Shanghai) was added, and the solution was stirred for another 24 h at room temperature. After centrifugation and washing by ethanol and PBS, the final product CTAC@Nb_2C-MSN-PEG-RGD was obtained.

Characterization

To obtain transmission electron microscopy (TEM) images, a JEM-2100F transmission electron microscope was used. High-resolution TEM (HRTEM), energy dispersive spectrum mapping (EDS) and electron energy loss spectroscopy (EELS) were performed to characterize the microstructure and composition of the planar nanoplatforms. A field-emission Magellan 400 microscope was operated to record scanning electron microscopy (SEM) images for morphology observation and corresponding elemental mapping analysis. A Rigaku D/MAX-2200 PX XRD system was used to acquire X-ray diffraction (XRD) patterns. X-ray photoelectron spectroscopy (XPS) was performed on a Thermal Scientific instrument (ESCAlab250). The zeta potential and hydrodynamic particle size were measured using a Nano ZS90 Zetasizer system. To obtain the BET surface area and corresponding pore volume and pore size, a Micrometitics Tristar 3000 system was used. To quantitatively analyze the contents of the nanosystems, an inductively coupled plasma-optical emission spectrometer (ICP-OES, Agilent 725) was operated. UV spectra were recorded using a UV-3600 Shimadzu spectrometer. A 1064 nm multimode pump laser was used for photothermal evaluation, which was purchased from Shanghai Connect Fiber Optics. An Olympus FV1000 was used to collect confocal laser scanning microscopy (CLSM) images. To investigate intracellular uptake of the nanosystems and the apoptosis status of the cancer cells, a BD LSRFortessa flow cytometer was operated.

Photothermal performance of CTAC@Nb_2C-MSN

The temperature fluctuations of Nb_2C and CTAC@Nb_2C-MSN during 808 nm and 1064 nm laser exposure were recorded using an infrared thermal camera (FLIR TM A325SC). Elevated Nb concentrations (31, 62.5, 125, 250 and 500 μg/mL) of Nb_2C and CTAC@Nb_2C-MSN dispersed in water were irradiated by 808 nm and 1064 nm lasers at a power intensity of 1.5 W/cm² for 5 min. Furthermore, the temperature changes of Nb_2C and CTAC@Nb_2C-MSN aqueous solutions at a Nb concentration of 500 μg/mL under irradiation by 808 nm and 1064 nm lasers at different power densities (0.5, 0.75, 1.0, 1.25 and 1.5 W/cm²) were also measured. Photothermal stability was tested by conducting three on/off cycles of laser irradiation of Nb_2C and CTAC@Nb_2C-MSN aqueous solution with prolonged durations.

Cell culture

U87 murine neuroglioma cells were used for *in vitro* and *in vivo* evaluations. The cells were bought from Shanghai Institute of Cells, Chinese Academy of Sciences. U87 cells were cultured in Dulbecco's Modified Eagle's Medium (DMEM, GIBCO), supplemented with penicillin/streptomycin (1%, GIBCO) and fetal bovine serum (FBS, 10%, GIBCO) in a manual incubator (5% CO_2, 37 °C). Cells were seeded in cell culture flasks (Corning) for 24 h to reach high confluency and then harvested by trypsin-EDTA solution (GIBCO).

In vitro cytotoxicity assay of Nb_2C-MSN-PEG and CTAC@Nb_2C-MSN-PEG

A standard CCK-8 cell viability assay (Sihai Bio-Tech, Shanghai, China) was used to determine the *in vitro* cytotoxicity of Nb_2C-MSN-PEG and CTAC@Nb_2C-MSN-PEG. Nb_2C-MSN-PEG and CTAC@Nb_2C-MSN-PEG at elevated concentrations (0, 18.75, 37.5, 75, 150 and 300 μg/mL) were incubated with U87 glioma cells that were pre-seeded in 96-well plates for 12 h. After 12 h and 24 h incubation, 10 μL CCK-8 solution diluted with 90 μL DMEM was added into a single well of each 96-well plate to evaluate cell viability using a microplate reader.

In vitro evaluation of the cytotoxicity of CTAC against U87 cells

To demonstrate the cytotoxicity of CTAC against U87 cells, 10^4 cells were pre-seeded in 96-well plates for 24 h. Then, CTAC was incubated with U87 cells at elevated concentrations (0, 15, 30, 60, 120 and 240

μg/mL) for 12 h and 24 h. CCK-8 solution diluted with DMEM containing FBS at a ratio of 1:9 was added to measure cell cytotoxicity using a microplate reader.

U87 cells were pre-seeded in 6-well plates for 24 h for apoptosis measurement of CTAC by flow cytometry. DMEM containing CTAC at elevated concentrations (0, 15, 30, 60, 120 and 240 μg/mL) was added and incubated with U87 cells for another 4 h. After cell dissociation, centrifugation and washing, the cells were dispersed into 500 μL binding buffer and stained with Annexin V FITC (5 μL) and PI (5 μL) (Dojindo Laboratorise). Then, flow cytometry was conducted to observe cell apoptosis stages.

In vitro enhanced chemotherapy and photothermal hyperthermia of cancer cells based on CTAC@Nb_2C-MSN-PEG-RGD

U87 cells were pre-seeded in 96-well plates at a density of 10^4 per well in DMEM containing 10% FBS at 37 °C for 24 h. CTAC, Nb_2C-MSN-PEG, CTAC@Nb_2C-MSN-PEG and CTAC@Nb_2C-MSN-PEG-RGD dispersions in DMEM were then added for another 12 h and 24 h incubation. To investigate the *in vitro* enhanced chemotherapy and PTT, the wells were divided into the following groups: control group, laser only group, Nb_2C-MSN-PEG only group, Nb_2C-MSN-PEG combined with laser group, CTAC only group, CTAC@Nb_2C-MSN-PEG group, CTAC@Nb_2C-MSN-PEG combined with laser group, CTAC@Nb_2C-MSN-PEG-RGD only group, and CTAC@Nb_2C-MSN-PEG-RGD combined with laser group. CCK-8 solution was added into each well and cell viabilities of the different treatment groups were calculated by comparing with the control group. All the laser-involved groups were exposed to 1064 nm laser at a power intensity of 1.0 W/cm^2 and 1.5 W/cm^2 for 5 min irradiation.

Intracellular endocytosis analysis

CLSM was performed to observe the intracellular uptake behavior of Nb_2C-MSN-PEG and Nb_2C-MSN-PEG-RGD into U87 cancer cells. The cancer cells were seeded into CLSM-specific culture dishes (NEST, Biotechnology Co., Ltd.) at a density of 10^5 cells per dish for 24 h and the medium was subsequently replaced by DMEM containing fluorescein isothiocyanate (FITC)-labeled Nb_2C-MSN-PEG (1 mL, 100 μg/mL) or FITC-labeled Nb_2C-MSN-PEG-RGD (1 mL, 100 μg/mL). The cells were then incubated for different durations (0 h, 1 h, 2 h and 4 h). 4',6-diamidino-2-phenylindole (DAPI, Beyotime Biotechnology, Beijing, China) was pre-mixed with methyl alcohol at a volume ratio of 1:10 for cell nucleus staining after incubation. After 20 min, the cells were gently washed with PBS and observed by CLSM.

For flow cytometry analysis, the cancer cells were pre-seeded into 6-well plates (5×10^5 cells per well). DMEM containing FITC-labeled CTAC@Nb_2C-MSN-PEG (3 mL, 100 μg/mL) or FITC-labeled CTAC@Nb_2C-MSN-PEG-RGD (3 mL, 100 μg/mL) was added into the plates to replace the previous medium and was then incubated for pre-determined time intervals (0 h, 1 h, 2 h and 4 h). Then, U87 cells were harvested by trypsin and collected into a test tube. The fluorescence signals of FITC-labeled CTAC@Nb_2C-MSN-PEG and FITC-labeled CTAC@ Nb_2C-MSN-PEG-RGD inside the cancer cells were measured by flow cytometry.

In vitro enhanced chemotherapy and photothermal hyperthermia as evaluated by CLSM and flow cytometry

U87 cancer cells were seeded into CLSM-specific dishes and cultured with DMEM medium containing FBS. After attachment onto the dishes, the medium was substituted by Nb_2C-MSN-PEG, CTAC@Nb_2C-MSN-PEG and CTAC@Nb_2C-MSN-PEG-RGD dispersions in DMEM (1 mL, 100 μg/mL), which were incubated for another 4 h. The dishes were subjected to different treatments: control group, laser only group, Nb_2C-MSN-PEG group, Nb_2C-MSN-PEG combined with laser group, CTAC@Nb_2C-MSN-PEG group, CTAC@Nb_2C-MSN-PEG combined with laser group, CTAC@Nb_2C-MSN-PEG-RGD group and CTAC@Nb_2C-MSN-PEG-RGD combined with laser group. 1064 laser irradiation was used in the experiment at a power density of 1.5 W/cm^2. After the aforementioned treatments, live (green) and dead (red) cells were stained by Calcein-AM (15 μL) and propidium iodide (PI, 12 μL) (Donjindo Molecular Technologies, Co., Ltd.) dispersed in PBS solution (7.5 mL) for 20 min. Finally, the U87 cells were gently washed with PBS and observed by CLSM.

Next, U87 cells were pre-seeded in 6-well plates for 24 h for apoptosis analysis by flow cytometry. DMEM containing CTAC, Nb_2C-MSN-PEG, CTAC@Nb_2C-MSN-PEG or CTAC@Nb_2C-MSN-PEG-RGD (3 mL, 100 μg/mL) was added into the cell plates and incubated for another 4 h. The cells were treated as mentioned above and were collected by trypsin-EDTA for cell dissociation. After centrifugation and washing with PBS twice, the cells were dispersed in 500 μL binding buffer and stained by Annexin V FITC (5 μL) and PI (5 μL) (Dojindo Laboratorise) for 20 min. Finally, flow cytometry was conducted to observe cell apoptosis status.

In vitro and *in vivo* photoacoustic (PA) imaging

To investigate the potential of CTAC@Nb_2C-MSN-PEG-RGD as a PA contrast agent, a Vivo LAZR photoacoustic imaging system (VisualSonics, Co., Ltd.) was used. CTAC@Nb_2C-MSN-PEG-RGD aqueous solution at elevated concentrations was tested (31.25, 62.5, 125, 250 and 500 μg/mL). Tumor-bearing nude mice were also used to evaluate the *in vivo* capability of CTAC@Nb_2C-MSN-PEG-RGD as a contrast agent for PA imaging. Mice were anesthetized by pentobarbital sodium (150 μL, mass ratio: 1%) *via* intraperitoneal injection. Finally, PA images were recorded before and after intravenous injection of CTAC@Nb_2C-MSN-PEG-RGD (dosage: 15 mg/kg) at intervals (0 min, 5 min, 15 min, 30 min, 1 h, 2 h, 4 h, 6 h, 8 h, 12 h and 24 h). The PA imaging parameters were set as: transducer frequency: 21 MHz; PA gain: 40 dB; focal depth: 12 mm.

Blood circulation, biodistribution and metabolism assessment of CTAC@Nb_2C-MSN-PEG-RGD

All animal experiments were conducted under guidelines approved by the Institutional Animal Care and Use Committe (IACUC) of Chongqing Medical University. 3×10^6 U87 cells were subcutaneously injected into the right side of the back of nude mice to establish a tumor model. For blood circulation analysis, 15 μL blood from mice (n = 3) was collected after intravenous injection of CTAC@Nb_2C-MSN-PEG-RGD at varied time points (2 min, 8 min, 15 min, 30 min, 1 h, 2 h, 4 h, 8 h, 12 h, 24 h). The Si concentration in the blood was measured by ICP-OES.

Biodistribution of CTAC@Nb_2C-MSN-PEG and CTAC@Nb_2C-MSN-PEG-RGD in the main organs and tumor tissues was studied in U87 tumor-bearing mice (n = 3 in each time point). Female tumor-bearing mice were injected with CTAC@Nb_2C-MSN-PEG or CTAC@Nb_2C-MSN-PEG-RGD *via* the tail vein. The mice were sacrificed at pre-arranged time points (2, 4 and 24 h). The major organs and tumor tissue were collected for subsequent weighing and dissolving in aqua regia. The Nb content in these samples was measured by ICP-OES and the distribution was calculated as the percent injected dose per gram of tissue (%ID/g). The biodistribution was calculated by following formula: Nb % (w/w) = (Nb in tissues/injected dose)/mass of tissue×100%.

To investigate the metabolism and excretion of CTAC@Nb_2C-MSN-PEG-RGD in U87 tumor-bearing mice (n = 3), CTAC@Nb_2C-MSN-PEG-RGD dispersed in saline was intravenously injected into mice and the urine and feces were collected at different time intervals (2, 6, 12, 24, 48 and 72 h). The Nb and Si contents were analyzed by ICP-OES.

In vivo enhanced chemotherapy and PTT by CTAC@Nb_2C-MSN-PEG-RGD

A U87 tumor xenograft model was established by subcutaneous injection (150 μL) of 10^7/mL U87 cancer cells dispersed in PBS at the right side of the back *via* a syringe. When the tumor volume reached around 50 mm^3, the mice were randomly divided into four groups: control group, laser only group, CTAC@Nb_2C-MSN-PEG-RGD only group, and CTAC@Nb_2C-MSN-PEG-RGD combined with laser group. The dose of CTAC@Nb_2C-MSN-PEG-RGD was set as 15 mg/kg. 4 h after intravenous injection, a 1064 nm laser was used to execute the therapeutic procedure at a power intensity of 1.5 W/cm^2. The length and width of the tumors were measured by a digital caliper every two day. The volume of tumor was calculated by the following formula: tumor volume (mm^3) = tumor length × tumor width^2 / 2. The inhibition ratio was calculated by the following formula: inhibition ratio = tumor volume of experimental group / tumor volume of control group × 100%.

After 15 days' treatment, the mice were euthanized and dissected to collect major organs and tumor tissues. The major organs were then stained by hematoxylin and eosin (H&E) to detect changes in their structure. The tumor regions were stained by H&E to observe the status of the U87 cells, terminal deoxynucleotidyl transferase dUTP nick-end labeling (TUNEL) to investigate DNA fragmentation during apoptosis, and Ki-67 antibody to observe cell proliferation after the different treatments. The weights of dissected tumor tissues were measured using a digital scale.

Statistical analysis

All data are shown as mean ± standard deviation (SD) and the significance levels between two groups' data were evaluated based on Student's two-tailed *t*-test (*$p < 0.05$, **$p < 0.01$, ***$p < 0.001$).

Results and discussion

Construction and characterization of a "therapeutic mesopore" coating on 2D Nb_2C MXenes

Compared to traditional mesoporous silica coatings on the surface of spherical nanoparticles [43-50], the surface engineering of 2D nanosheets is relatively challenging because of their ultrathin planar topology that is easily influenced by lots of factors such as planar size, dispersity, synthetic parameters, *etc* [52,53]. It has been demonstrated that the surface of 2D MXenes is covered with abundant -OH groups, which makes the surface charge of these nanosheets

negative [35,54]. Based on this fact, the positively charged surfactant cetanecyltrimethylammonium chloride (CTAC) was pre-introduced to self-assemble onto the surface of Nb_2C MXenes *via* electrostatic interactions (**Figure 1A**). Then, the organosilica source (tetraethylorthosilicate, TEOS) was added into the reaction system. The hydrolyzed/condensed oligomers from TEOS further self-assembled with the surfactant micelles to form mesoporous-silica shells on the surface of 2D Nb_2C MXenes (designated as CTAC@Nb_2C-MSN**)**. The traditional strategy is to remove the surfactants by either extraction or calcination, by which mesopores are produced as reservoirs to load other therapeutic agents [55-59]. Significantly different from this traditional strategy, this work kept the surfactant micelles within the mesopores, where these surfactant molecules were directly used as the chemotherapeutic agents [60,61]. This design protocol was based on a previous report that positively charged surfactants as mesopore-making agents could be directly used as drug molecules for efficient killing of cancer cells [61]. Therefore, this methodology avoids the tedious surfactant removal and post drug-loading steps, which is more practical for further large-scale production. In addition, it can achieve a high drug loading capacity because the mesopores are almost fully filled with surfactant in the form of self-assembled micelles during the synthesis.

Another important advantage of the mesoporous silica coating is the abundant saline chemistry present on the surface of CTAC@Nb_2C-MSN composite nanosheets, making further surface engineering possible. As a first step, PEGylation was adopted to guarantee high stability of these nanosheets in physiological conditions, which is of high significance for *in vivo* applications. Initially, the silanol (Si-OH) group on the surface of the composite nanosheets was used for reaction with (3-aminopropyl) triethoxysilane (APTES) to make the surface abundant with amino groups, followed by reaction with NHS-PEG-MAL. Next, an RGD peptide was conjugated onto the surface of the composite nanosheets to endow them with high specificity to recognize and bind integrin $\alpha_v\beta_3$, which is overexpressed on cancer cell membranes. These

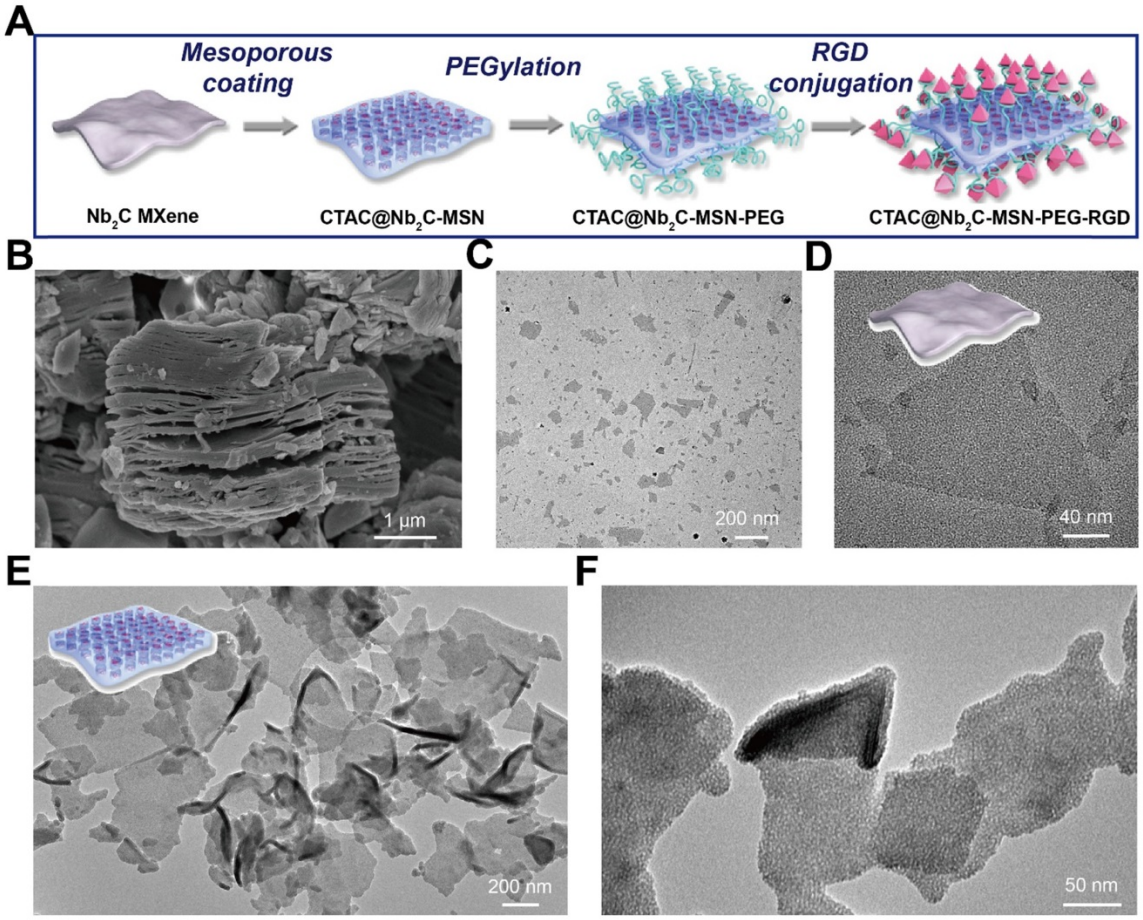

Figure 1. Synthesis and characterization of core/shell-structured CTAC@Nb_2C-MSN. (A) The scheme of the synthetic procedure and stepwise surface PEGylation/targeting modification of CTAC@Nb_2C-MSN. **(B)** SEM image of Nb_2C MXene as-synthesized by the first-step HF etching. **(C)** Low- and **(D)** high-magnification TEM images of as-synthesized Nb_2C MXene nanosheets. **(E)** Low- and **(F)** high-magnification TEM images of CTAC@Nb_2C-MSN composite nanosheets. Inset of (E): scheme of the microstructure of CTAC@Nb_2C-MSN.

stepwise surface PEGylation and targeting modifications (**Figure 1A**) are difficult to achieve on the surface of traditional bare 2D Nb_2C MXenes because of the absence of useful functional groups. Comparatively, it is easy and feasible to realize this surface silica coating protocol because of the versatile saline chemistry.

Layer-structured Nb_2AlC bulk ceramics were initially etched by 50% HF to remove the Al layer within the crystal structure. SEM (**Figure 1B**) demonstrates that the interlayer space was obviously enlarged by the HF etching, showing an obvious layered nanostructure after HF etching. Because of their stacked layers and large planar size, bulk ceramics are not optimal for biomedical applications, especially for intravenous administration where large aggregates would block blood vessels and cause a high biosafety risk. Therefore, the following exfoliation step was adopted by choosing the typical tetrapropylammonium hydroxide (TPAOH) as the exfoliation agent. It was found that this TPAOH exfoliation step induced complete intercalation and exfoliation of the Nb_2C MXene nanosheets (**Figure 1C-D**). In particularly, the post exfoliation step decreased the planar size of the nanosheets, making these MXene nanosheets feasible for biomedical applications where a small planar size is typically required. Importantly, the two-step exfoliation approach still retained the high crystallinity of these Nb_2C MXene nanosheets (**Figure S1** and **Figure S2**), indicating that their physiochemical properties would be kept after the exfoliation. A uniform mesoporous silica layer was clearly distinguished on the surface of Nb_2C MXene in CTAC@Nb_2C-MSN (**Figure 1E-F**). Especially, all these MXene nanosheets were covered by a mesoporous silica layer without additional homogenous nucleation of silica nanoparticles in the system, indicating the high efficacy and specificity of this coating procedure. Importantly, the initial 2D planar topology remained after the surface-mesopore coating procedure.

The presence of abundant mesopores on the surface of CTAC@Nb_2C-MSN composite nanosheets was clearly identified by high-resolution SEM (**Figure 2A** and **Figure S3**). These mesopores penetrate through the whole matrix with opening pores on the surface, which is the characteristic structure of representative mesoporous materials. To characterize the structure and composition of CTAC@Nb_2C-MSN in detail, a single CTAC@Nb_2C-MSN nanosheet was chosen for versatile characterizations, including SEM (**Figure 2B**), dark-field TEM (**Figure 2C**), bright-field TEM (**Figure 2D**) and corresponding element mapping such as Nb element (**Figure 2E**), Si element (**Figure 2F**) and O element (**Figure 2G**). Both SEM and TEM images clearly show the unique mesoporous structure in the whole planar matrix where both Nb and Si elements co-exist, demonstrating the desirable mesoporous structure, hybrid composition and 2D planar topology.

X-ray photoelectron spectroscopy (XPS) was used to determine the element-valence status of 2D Nb_2C before and after mesoporous coating. Compared to the XPS spectrum of 2D Nb_2C, the spectrum of Nb_2C-MSN shows new Si signals because of the silica coating (**Figure 3A-C**). The presence of Nb-O bond is attributed to the partial oxidation of Nb_2C MXene (**Figure 3B** and **Figure S4**). No Al element signal can be observed, suggesting that no residual Al remained after two-step etching. The O 1s spectrum further demonstrates the presence of Si-O and Nb-O bonds in Nb_2C-MSN (**Figure 3D**). The average particle size of CTAC@Nb_2C-MSN is around 122.4 nm as tested by dynamic light scattering (DLS), which increased to 220.2 nm by further PEGylation and RGD conjugation (**Figure S5**). In addition, CTAC@Nb_2C-MSN-PEG-RGD could be easily dispersed into various physiological solutions (**Figure S6**) such as deionized water, Dulbecco's Modified Eagle Medium (DMEM), saline, simulated body fluid (SBF) and phosphate buffered saline (PBS) with high colloidal stability to guarantee further *in vivo* biomedical use. The presence of mesopores on the surface of the silica layer was further characterized by the N_2 absorption-desorption technique. It was found that CTAC@Nb_2C-MSN shows a low BET surface area and pore volume of only 21.69 m^2/g and 0.09 cm^3/g, respectively, which is attributed to the occupation of the mesopores by CTAC micelles. After the removal of CTAC within the mesopores by extraction, the Nb_2C-MSN composite nanosheets exhibited a high BET surface area and pore volume of 309.93 m^2/g and 0.59 cm^3/g, respectively, further demonstrating the successful surface mesopore coating and CTAC loading within the mesopore (**Figure 3E**). The mesopore size was also enlarged by the CTAC removal (**Figure 3F**). The drug (CTAC)-loading capacity was determined by thermogravimetric analysis (**Figure 3G**), from which the CTAC loading was calculated to be as high as 32.57% (**Figure 3H**), indicating the high efficacy of this strategy for drug loading and potential for efficient chemotherapy. Therefore, this multifunctional 2D composite nanoplatform is expected to exert the specific functionalities of photo-responsive for simultaneous photothermal hyperthermia and chemotherapy (**Figure 3I**).

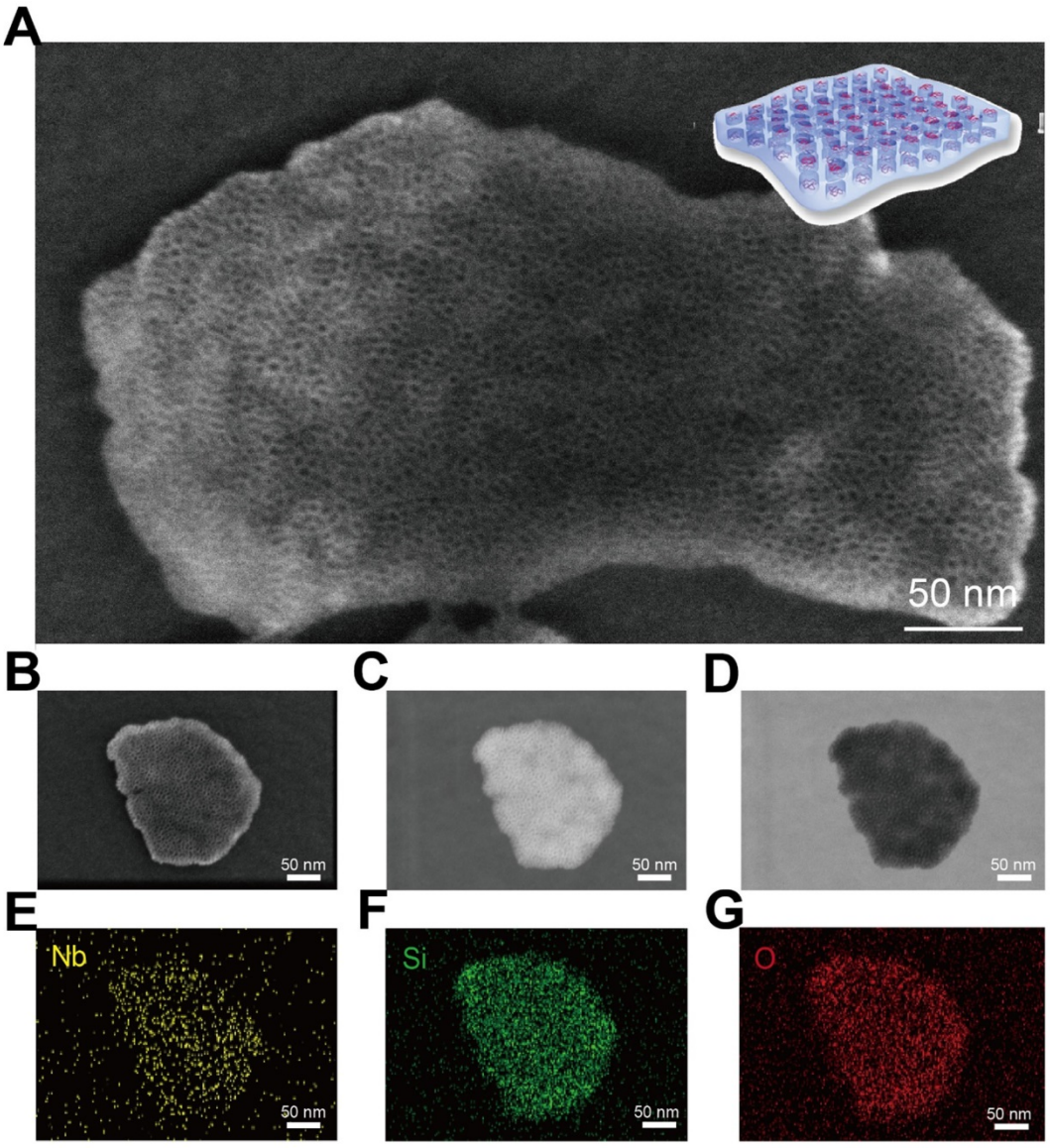

Figure 2. Morphology, microstructure and composition characterization of core/shell-structured CTAC@Nb_2C-MSN. (A) High-resolution SEM image of CTAC@Nb_2C-MSN composite nanosheets. **(B-G)** Detailed characterization of a single CTAC@Nb_2C-MSN composite nanosheet, including (B) SEM image, (C) dark-field TEM image, (D) bright-field TEM image and (E-G) corresponding element mapping of the same nanosheet (e: Nb, f: Si, and g: O elements). Scale bars of (B-G) are 50 nm.

The therapeutic mesoporous-silica coating maintains the high photothermal conversion capability of 2D Nb_2C MXenes. UV-vis-NIR spectra of CTAC@Nb_2C-MSN show strong photo-absorption in the NIR range, even in the second biowindow (**Figure 4A**). It has been demonstrated that the second biowindow has deeper tissue penetration as compared to the first biowindow, but the deficiency of photothermal agents is a significant challenge for photo-therapy [41]. This work reports, for the first time, the construction of 2D mesoporous nanocomposites with specific photo-therapeutic functionality in the NIR-II biowindow. The extinction coefficient of CTAC@Nb_2C-MSN is calculated to be 9.71 $L \cdot g^{-1} \cdot cm^{-1}$ in the NIR-II biowindow (inset of **Figure 4A**), which is significantly higher than traditional 2D graphene oxide as the photothermal nanoagent in the NIR-I biowindow (3.6 $L \cdot g^{-1} \cdot cm^{-1}$) [62]. In addition, the photothermal conversion performance of CTAC@Nb_2C-MSN was investigated at different concentrations (31, 62.5, 125, 250 and 500 μg/mL) by exposing aqueous solutions to NIR-II laser (1064 nm) at a power density of 1.5 W/cm^2 (**Figure 4B**). The temperature reached as high as 67.3 °C, which is sufficiently high to kill cancer cells. The temperature elevation at increased power densities of 1064 nm laser (0.5, 0.75, 1.0, 1.25 and 1.5 W/cm^2) indicates that such a thermal effect is powder density dependent (**Figure 4C**). In addition, there is no distinct change on the thermal effect of CTAC@Nb_2C-MSN composite nanosheets during three laser on-off heating cycles (**Figure 4D**),

indicating their relatively high photothermal stability. Finally, the photothermal conversion efficiency (η) is calculated to be 28.6% based on the maximum heating temperature (**Figure 4E**) and the time constant for heat transfer (**Figure 4F**), which is higher than that reported of typical Au nanorods (21%) [63] and Cu_{2-x}-Se nanocrystals (22%) [64], indicating the high photothermal efficacy of these composite nanosheets for photo-hyperthermia. In addition, the photothermal performance of these composite nanosheets was assessed in the NIR-I biowindow (λ = 808 nm, **Figure S7**), which indicated that these nanosheets also feature photothermal conversion performance in the NIR-I biowindow. Importantly, the photothermal performance of Nb_2C nanosheets had no obvious change before and after silica-shell coating in both the NIR-I (λ = 808 nm, **Figure S8**) and NIR-II biowindows (λ= 1064 nm, **Figure S9**).

In vitro targeted and enhanced chemotherapy and PTT against U87 cancer cells

Both the mesoporous silica shell and 2D Nb_2C MXene core in CTAC@Nb_2C-MSN-PEG-RGD have therapeutic functions (**Figure 5A**). The U87 brain cancer cell line with cell membrane overexpression of integrin $\alpha_v\beta_3$ was used for the following *in vitro* and *in vivo* assessments; the cells can be specifically recognized by surface-conjugated RGD on CTAC@Nb_2C-MSN-PEG-RGD. Upon endocytosis into the cancer cells, CTAC within the mesopores gradually releases for chemotherapy. The introduction of laser irradiation in the NIR-II biowindow (1064 nm) activates the Nb_2C core for photothermal conversion, which elevates the temperature of the tumor cells for photothermal hyperthermia. To show the therapeutic functionality of CTAC, it was pre-extracted from the mesopores (Nb_2C-MSN-PEG-RGD). It was found that Nb_2C-

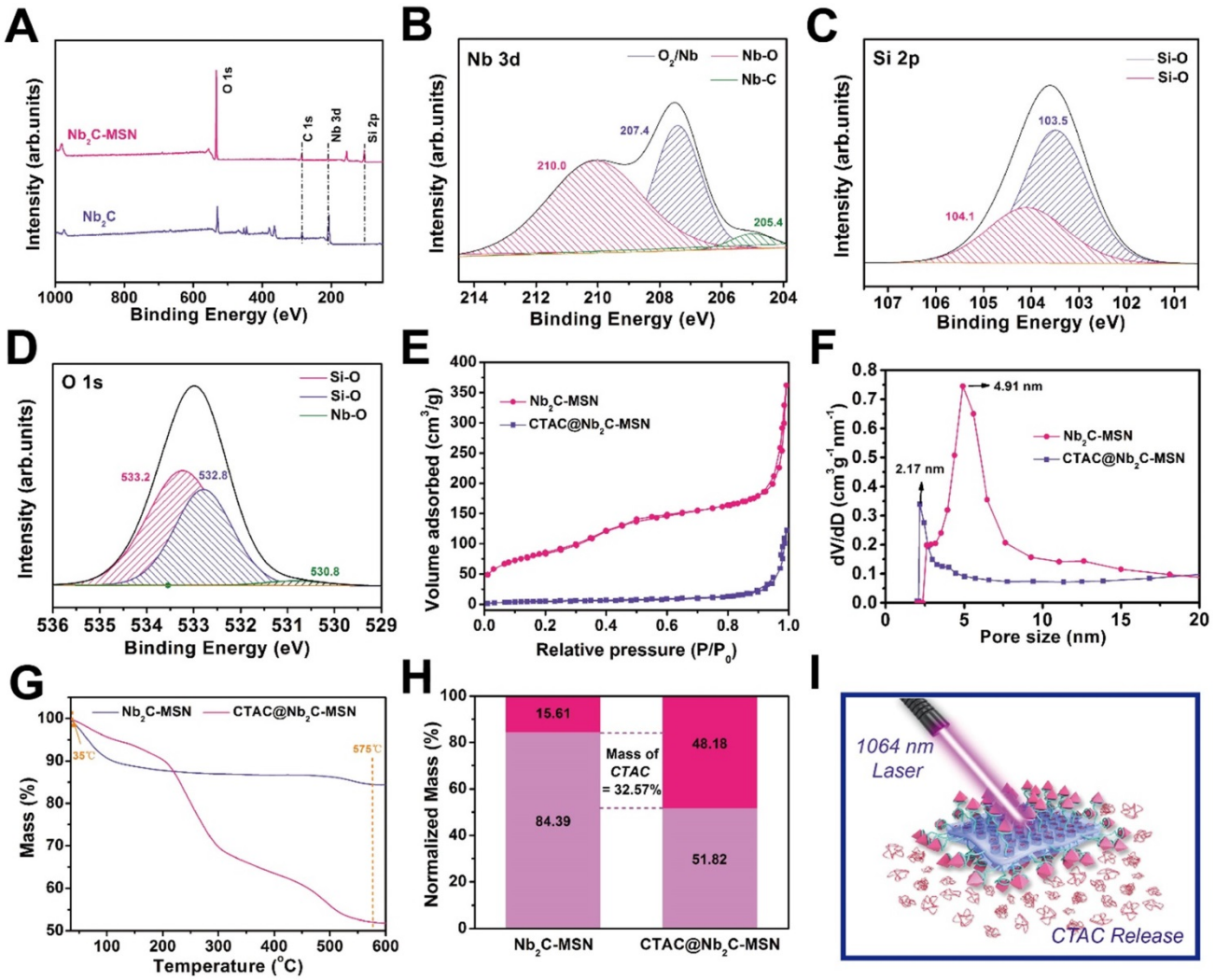

Figure 3. Structural and compositional characterizations of CTAC@Nb_2C-MSN nanosheets. (A) XPS spectra of Nb_2C and Nb_2C-MSN. Fitted **(B)** Nb 3d, **(C)** Si 2p and **(D)** O 1s XPS spectra of Nb_2C-MSN. **(E)** N_2 adsorption−desorption isotherms and **(F)** corresponding pore-size distributions of Nb_2C-MSN and CTAC@Nb_2C-MSN. **(G)** Thermogravimetric analysis (TGA) and **(H)** normalized weight loss reduction of Nb_2C@MSN and CTAC@Nb_2C-MSN. **(I)** The scheme of photo-triggered response for photothermal hyperthermia and CTAC release for chemotherapy based on CTAC@Nb_2C-MSNs-PEG-RGD composite nanosheets.

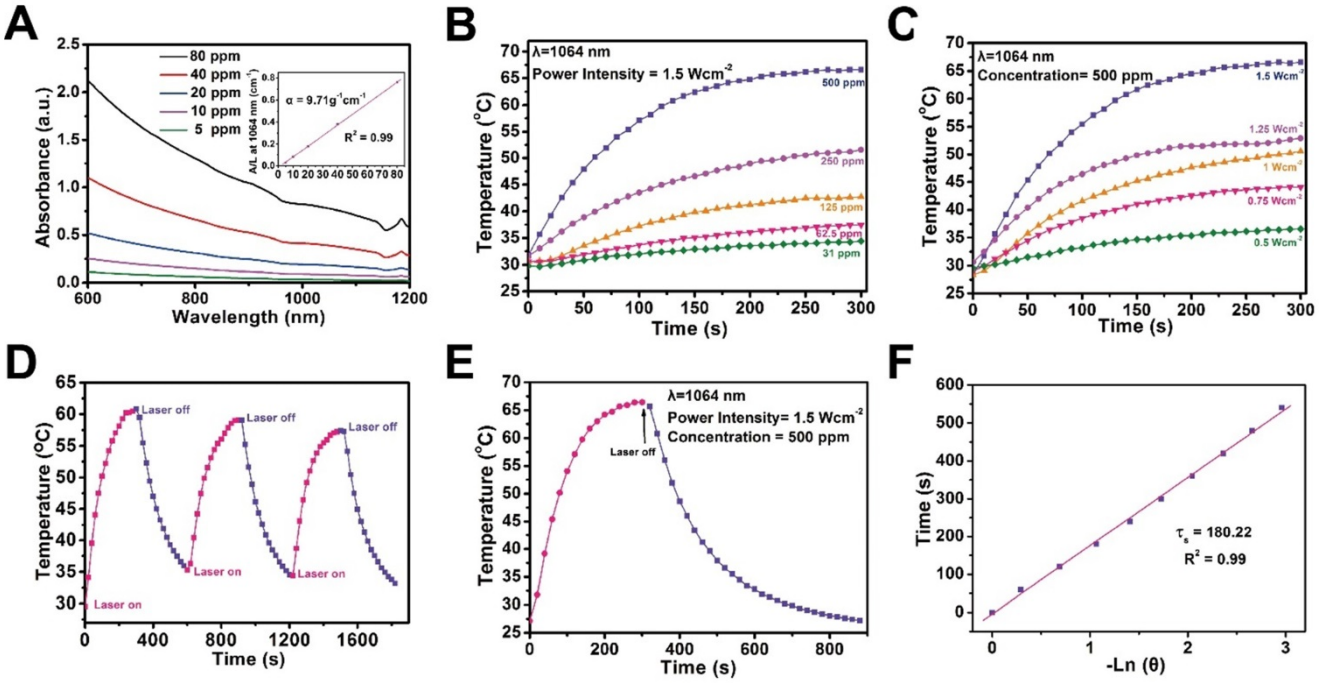

Figure 4. ***In vitro*** **photothermal conversion assessment of CTAC@Nb_2C-MSN. (A)** UV-vis spectra of CTAC@Nb_2C-MSN at different concentrations (5, 10, 20, 40 and 80 μg/mL) in aqueous solution. Inset: mass extinction coefficient of CTAC@Nb_2C-MSN at λ = 1064 nm. Normalized absorption intensity at 1064 nm divided by length of the cell (A/L). **(B)** Temperature changes of CTAC@Nb_2C-MSN aqueous solution with NIR-II laser (1064 nm, power density: 1.5 W/cm²) irradiation at elevated concentrations (31, 61.5, 125, 250 and 500 μg/mL). **(C)** Photothermal heating curves of CTAC@Nb_2C-MSN dispersed in aqueous solution irradiated by different power intensities (0.5, 0.75, 1.0, 1.25 and 1.5 W/cm²) of NIR-II laser at the wavelength of 1064 nm. **(D)** Heating curve of CTAC@Nb_2C-MSN dispersed in water for three laser on/off cycles irradiated by a 1064 nm laser at the power intensity of 1.5 W/cm². **(E)** Photothermal performance of CTAC@Nb_2C-MSN dispersed in aqueous solution under NIR irradiation; the laser was turned off when the temperature was stable. **(F)** Time constant for heat process transfer calculated from the cooling period.

MSN-PEG shows no obvious cytotoxicity even at a high concentration of 300 μg/mL after incubation with cancer cells for 12 h and 24 h (**Figure 5B**). In contrast, the presence of CTAC in CTAC@Nb_2C-MSN-PEG induced concentration-dependent cytotoxicity (**Figure 5C**), demonstrating the high chemotherapeutic efficacy of CTAC as a chemodrug within the mesopores. To evaluate the cytotoxicity of CTAC, an elevated concentration of CTAC was incubated with U87 cells. As shown in **Figure 5D**, the cell viability exhibited concentration-dependent and incubation time-dependent behaviour after incubation with CTAC. Furthermore, the results were corroborated by flow cytometry to analyze apoptosis of cancer cells (**Figure 5E**) and corresponding quantitative measurements (**Figure 5F**).

To reveal the targeting capability of surface-conjugated RGD, FITC-labeled Nb_2C-MSN-PEG (without RGD-targeting modification) and Nb_2C-MSN-PEG-RGD (with RGD-targeting modification) were incubated with U87 cells (for 1 h, 2 h and 4 h). It was found that the cancer cells after incubation with FITC-labeled Nb_2C-MSN-PEG-RGD showed substantially higher intracellular green fluorescence as compared to the cancer cells after incubation with FITC-labeled Nb_2C-MSN-PEG (**Figure 6A**). In particularly, in a competition experiment after pre-incubation of cells with free RGD there was decreased intracellular uptake of FITC-labeled Nb_2C-MSN-PEG-RGD because of the occupation of cell membrane-overexpressed integrin $\alpha_v\beta_3$ by pre-introduced free RGD. In addition, flow cytometry was conducted to further quantitatively determine the intracellular uptake behavior and targeting efficacy of these nanosheets. CTAC@Nb_2C-MSN-PEG-RGD (**Figure 6B**) exhibited significantly enhanced intracellular uptake as compared to CTAC@Nb_2C-MSN-PEG without RGD-targeting modification (**Figure 6C**). The results of uptake percentage (**Figure 6D**) also demonstrate that the surface-linked RGD is favorable for the intracellular uptake of these composite nanosheets, which also indirectly indicates the functionality of the mesoporous silica layer that makes the surface engineering of MXene-based nanosheets possible.

Furthermore, the enhanced therapeutic efficacy (chemotherapy and PTT) of CTAC@Nb_2C-MSN-PEG-RGD upon external laser irradiation in the NIR-II biowindow (1064 nm) was evaluated against U87 cancer cells with the following treatment groups: control (without treatment), laser only, Nb_2C-MSN-PEG only, Nb_2C-MSN-PEG combined with laser irradiation, CTAC@Nb_2C-MSN-PEG only, CTAC@Nb_2C-MSN-PEG combined with laser irradiation, CTAC@Nb_2C-MSN-PEG-RGD only, CTAC@Nb_2C-MSN-PEG-RGD combined with laser

irradiation. The laser only and Nb_2C-MSN-PEG only (without CTAC) groups had no obvious cytotoxicity. Comparatively, CTAC@Nb_2C-MSN-PEG-RGD showed higher cell toxicity as compared to CTAC@Nb_2C-MSN-PEG because of the targeting effect. Importantly, the CTAC@Nb_2C-MSN-PEG-RGD combined with laser irradiation group exhibited the highest cytotoxicity as compared to both CTAC@Nb_2C-MSN-PEG-RGD only group (chemotherapy) and CTAC@Nb_2C-MSN-PEG-RGD combined with laser irradiation group (PTT), demonstrating enhanced efficacy (**Figure 6E** and **Figure S10**) based on the specific functionalities of both the mesoporous silica layer (loading CTAC for chemotherapy) and Nb_2C MXene core (photothermal conversion for PTT). It is notable that this strategy simply employs the *in situ* self-assembled CTAC within the mesopores as the chemotherapeutic agent rather than traditional surfactant extraction and further chemodrug loading. In addition, the surface RGD targeting increased the uptake of these planar nanocomposites into cancer cells to further enhance therapeutic efficacy. Furthermore, both flow cytometry for analysis of apoptosis of cancer cells (**Figure 6F-G**) and CLSM observation of live/dead cells (**Figure 6H**) demonstrate that CTAC@Nb_2C-MSN-PEG-RGD combined with laser irradiation exhibited the highest therapeutic efficacy for inducing cancer cell apoptosis and death.

In vitro and *in vivo* PA imaging

Typically, photothermal nanoagents are featured with performance in photoacoustic (PA) imaging [65-69], which is also expected for CTAC@Nb_2C-MSN-PEG-RGD composite nanosheets because of their high photothermal conversion capability. To demonstrate this assumption, a set of experiments on a PA imaging system was conducted. The *in vitro* high

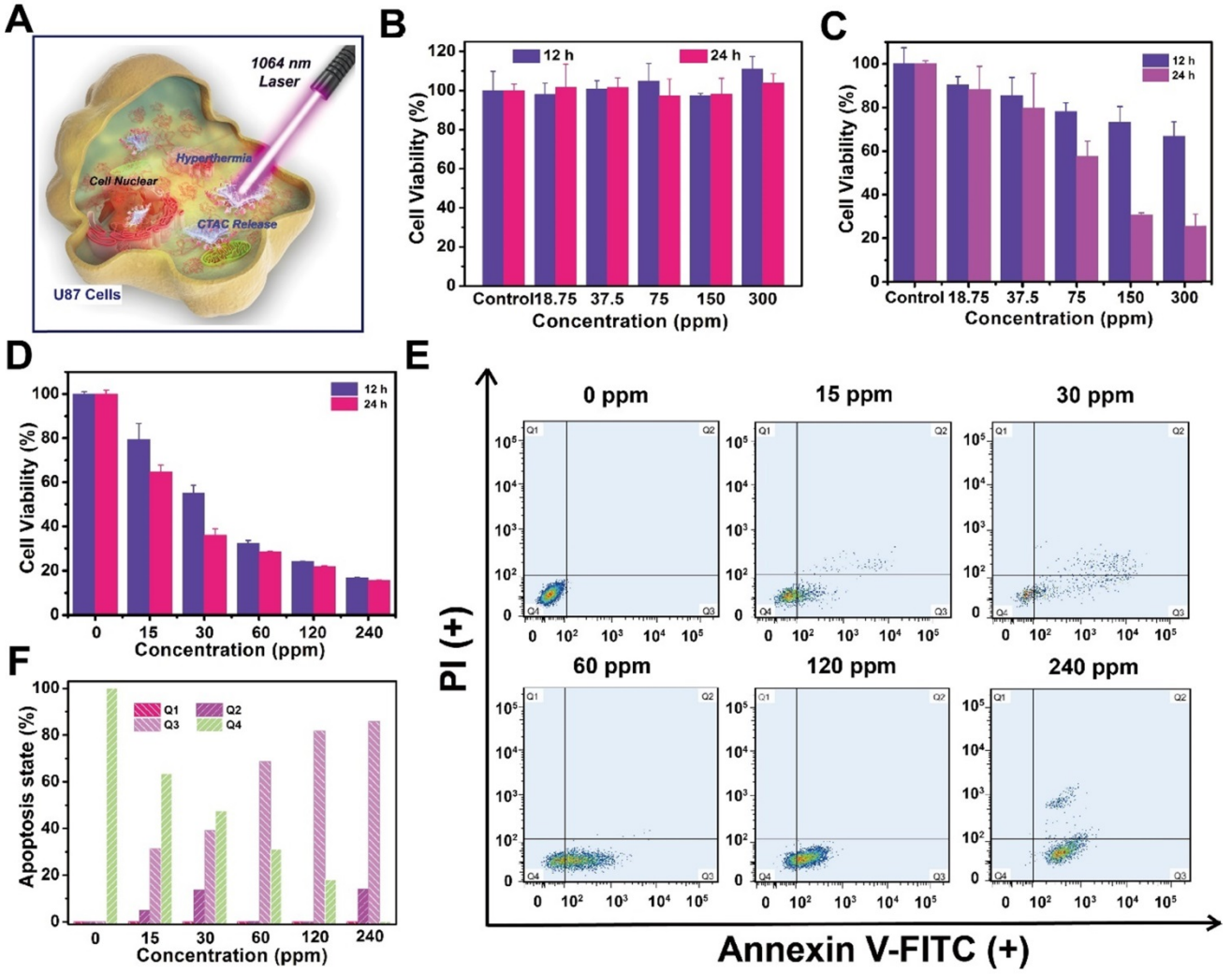

Figure 5. ***In vitro*** **CTAC cytotoxicity against U87 cancer cells. (A)** Schematic illustration of CTAC@Nb_2C-MSN-PEG-RGD for enhanced chemotherapy and PTT against cancer cells. Relative cell viability of U87 cancer cells after incubation with **(B)** Nb_2C-MSN-PEG, **(C)** CTAC@Nb_2C-MSN-PEG and **(D)** CTAC at elevated concentrations for 12 h and 24 h. **(E)** Flow-cytometry apoptosis assay of U87 cells after incubation with CTAC at different concentrations followed by staining with Annexin-FITC and PI, and **(F)** corresponding quantitative analysis of U87 cells at different stages (Q1: dead cells; Q2: late apoptotic cells; Q3: early apoptotic cells; Q4: live cells).

PA signal intensity can be observed in **Figure 7A** at a range from 680 nm to 900 nm, and the PA values depend linearly on the concentration of CTAC@Nb_2C-MSN-PEG-RGD (**Figure 7B**).

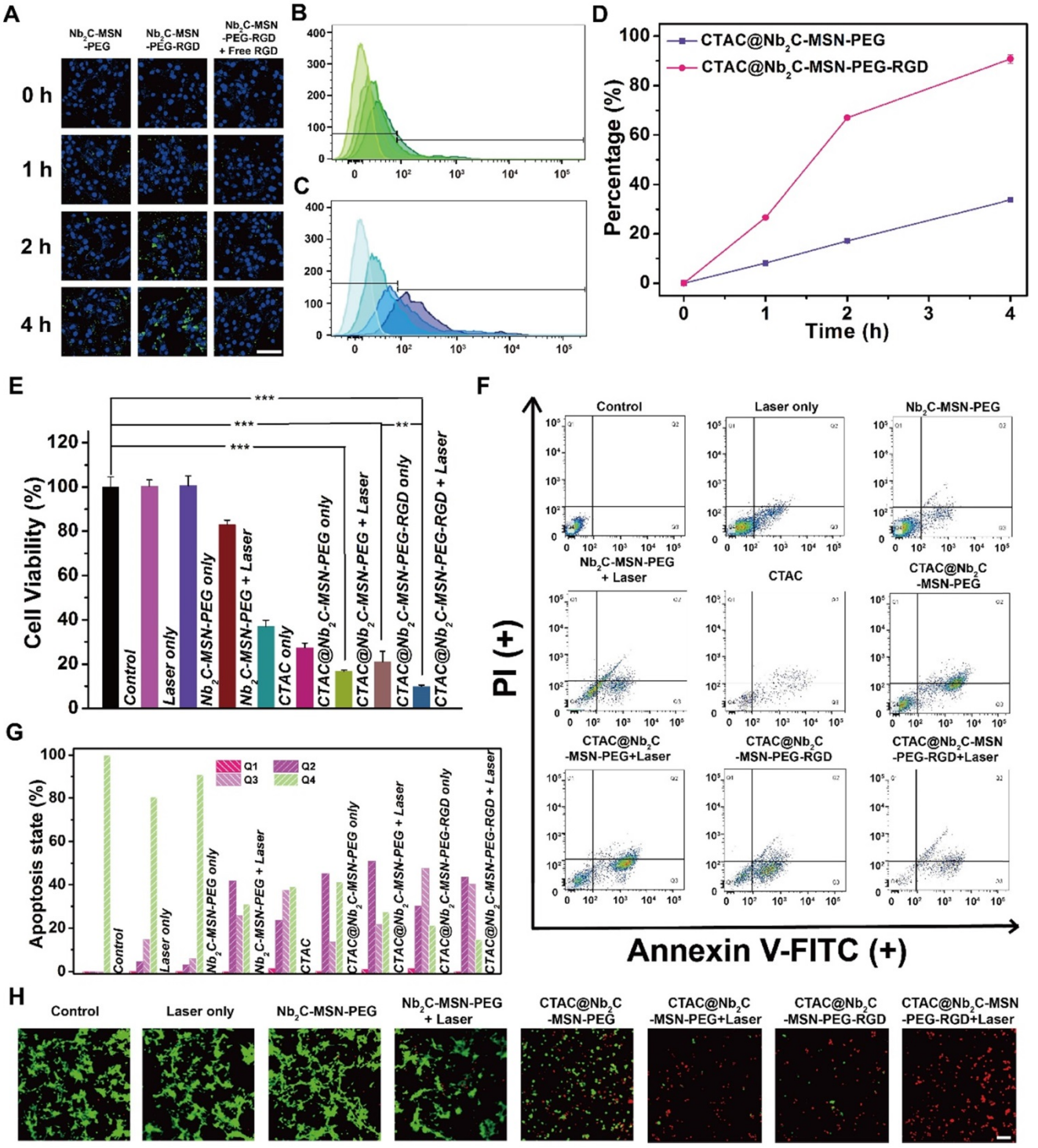

Figure 6. ***In vitro*** **chemo/PTT-based enhanced cancer therapy against U87 cancer cells. (A)** CLSM images of U87 cells incubated with FITC-labeled Nb_2C-MSN-PEG and Nb_2C-MSN-PEG-RGD at a concentration of 100 μg/mL for 0, 1, 2 and 4 h. Scale bar: 40 μm. Flow cytometry result of intracellular uptake of **(B)** FITC-labeled CTAC@Nb_2C-MSN-PEG and **(C)** CTAC@Nb_2C-MSN-PEG-RGD after incubation with U87 cells for different time intervals (0, 1, 2 and 4 h) and **(D)** corresponding uptake percentage analysis to show the targeting efficacy. **(E)** Relative cell viability of U87 cells after 24 h incubation by different treatments, including control (without treatment), laser only, Nb_2C-MSN-PEG only, Nb_2C-MSN-PEG combined with laser irradiation, CTAC only group, CTAC@Nb_2C-MSN-PEG only, CTAC@Nb_2C-MSN-PEG combined with laser irradiation, CTAC@Nb_2C-MSN-PEG-RGD only, and CTAC@Nb_2C-MSN-PEG-RGD combined with laser irradiation (**P < 0.01, ***P < 0.001). The scale bar is 40 μm. **(F)** Flow cytometry apoptosis assay of U87 cells under different treatments followed by staining with Annexin-FITC and PI and **(G)** corresponding quantitative analysis of U87 cells at different stages (Q1: dead cells; Q2: late apoptotic cells; Q3: early apoptotic cells; Q4: live cells). **(H)** CLSM images of U87 cells after different treatments, followed by staining with PI (red fluorescence) and calcein-AM (green fluorescence) (Scale bar: 40 μm).

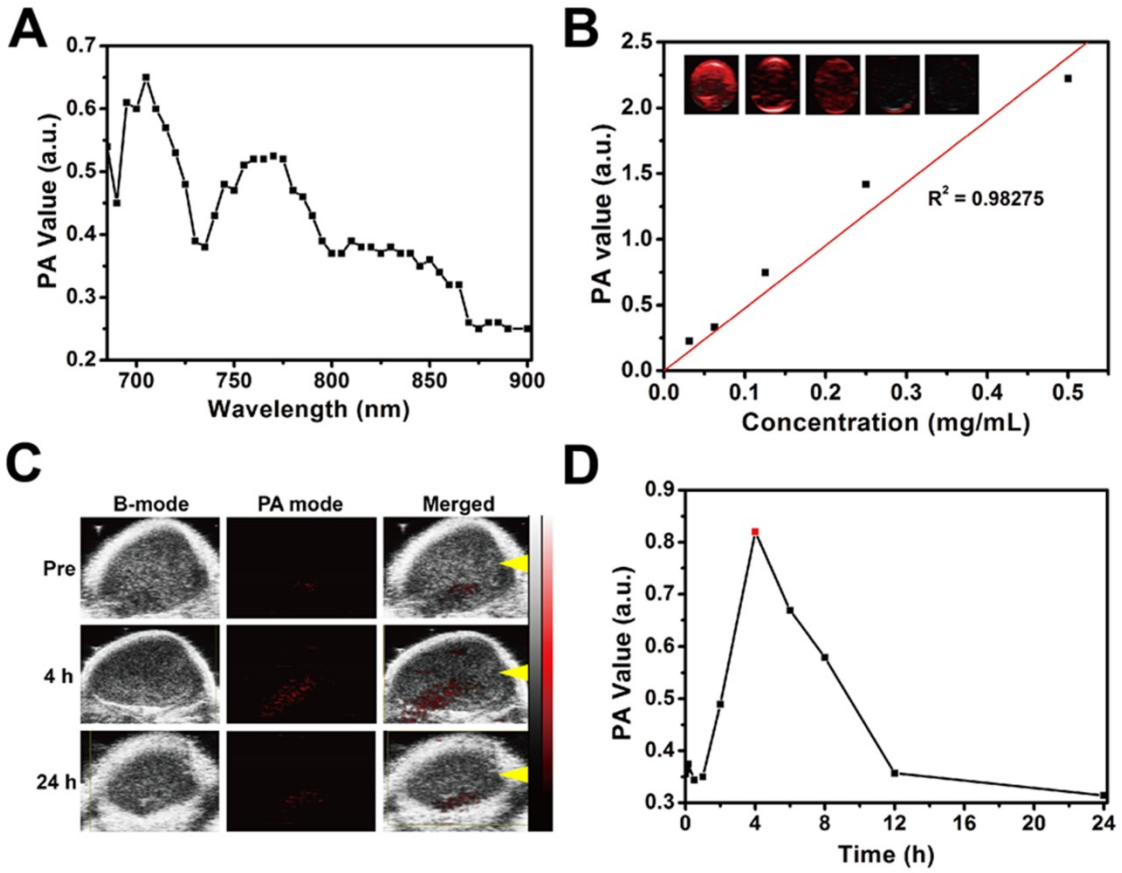

Figure 7. ***In vitro*** **and** ***in vivo*** **PA imaging performance of CTAC@Nb_2C-MSN-PEG-RGD. (A)** PA signal intensity of CTAC@Nb_2C-MSN-PEG-RGD at varied wavelengths of laser excitation. **(B)** PA signal intensity of CTAC@Nb_2C-MSN-PEG-RGD at elevated concentrations (0, 31.25, 62.5, 125, 250 and 500 μg/mL), and (inset image) corresponding *in vitro* PA images of CTAC@Nb_2C-MSN-PEG-RGD. **(C)** *In vivo* 2D ultrasound images, PA images and merged ultrasound and PA images of the tumor region (yellow arrow means the focal depth of the PA transducer) after intravenous administration of CTAC@Nb_2C-MSN-PEG-RGD *via* the tail vein at different time points (pre, 4 h, and 24 h), and **(D)** the corresponding quantitative changes in PA signal intensity.

The *in vivo* PA imaging property of CTAC@Nb_2C-MSN-PEG-RGD was then evaluated. Tumor-bearing mice were injected with CTAC@Nb_2C-MSN-PEG-RGD *via* the tail vein and PA images were taken at different time intervals after the injection. It was found that CTAC@Nb_2C-MSN-PEG-RGD gradually accumulates into the tumor tissue and generates obvious PA signal in the tumor (**Figure 7C**), which was further reveled by quantitative PA signal measurement (**Figure 7D**). These desirable *in vitro* and *in vivo* data strongly demonstrate the high potential of CTAC@Nb_2C-MSN-PEG-RGD as a contrast agent for PA imaging, providing the potential for guidance and monitoring of enhanced therapies by these 2D composite nanosheets.

In vivo targeted and enhanced chemotherapy and PTT of U87 tumor xenograft

During *in vivo* enhanced therapeutic applications, CTAC@Nb_2C-MSN-PEG-RGD composite nanosheets initially extravasate into the tumor tissue by passive targeting *via* the enhanced permeability and retention (EPR) effect, and then are preferentially taken up by cancer cells *via* RGD recognition (**Figure 8A**). Upon arriving at the tumor tissue, CTAC gradually releases from the composite nanosheets for chemotherapy. Laser irradiation in the NIR-II biowindow activates the Nb_2C core in CTAC@Nb_2C-MSN-PEG-RGD for photothermal conversion, which quickly increases the temperature of the tumor tissue and induces tumor photothermal ablation. The blood circulation of CTAC@Nb_2C-MSN-PEG-RGD was initially evaluated, and its half-life in the bloodstream was calculated to be 55.6 min (**Figure 8B**). In addition, its clearance rate in the first 2 h was (0.40 μg/mL/h), which is much higher (**Figure 8C**) than that of the following 22 h (0.03 μg/mL/h).

To show the *in vivo* targeting efficacy, both CTAC@Nb_2C-MSN-PEG-RGD (with RGD targeting) and CTAC@Nb_2C-MSN-PEG (without RGD targeting) were intravenously administrated into U87 subcutaneous tumor-bearing mice. It was found (**Figure 8D**) that CTAC@Nb_2C-MSN-PEG-RGD efficiently accumulated into the tumor tissue with targeting efficacies of 5.47%, 9.57% and 5.75% at 2 h, 4 h and 24 h after intravenous injection, respectively. In

comparison, the intravenous administration of CTAC@Nb_2C-MSN-PEG without RGD-targeting function achieved much lower targeting efficacies of 2.05%, 4.20% and 1.32% at 2 h, 4 h and 24 h after administration, respectively. This result demonstrates that the RGD-targeting design on the surface of the composite nanosheets favors their accumulation into tumor tissue, which could guarantee further enhanced therapeutic treatment.

Upon laser irradiation in the NIR-II biowindow, the temperature of the tumor tissue elevated rapidly after intravenous administration of CTAC@Nb_2C-MSN-PEG-RGD composite nanosheets (**Figure 8E-F**). The surface temperature of the tumor reached as high as 52.3 °C after 10 min of irradiation, which was sufficiently high to ablate the tumor tissue. Comparatively, the tumor temperature did not obviously increase without injection of these composite nanosheets, further indicating the functionality of CTAC@Nb_2C-MSN-PEG-RGD composite nanosheets for assisting photothermal conversion. After the photothermal hyperthermia and continuous chemotherapy, the status of tumor-bearing mice and the tumor tissue was monitored during the following fifteen days, where significantly enhanced tumor suppression was observed in tumor-bearing mice after treatment with CTAC@Nb_2C-MSN-PEG-RGD composite nanosheets followed by NIR-II laser irradiation (**Figure 8G**).

Systematic *in vivo* therapeutic evaluation was then assessed in treatment groups of control, laser only, CTAC@Nb_2C-MSN-PEG-RGD, and CTAC@ Nb_2C-MSN-PEG-RGD combined with laser irradiation in the NIR-II biowindow (1064 nm). The body weights of tumor-bearing mice after different treatments showed no significant variation (**Figure**

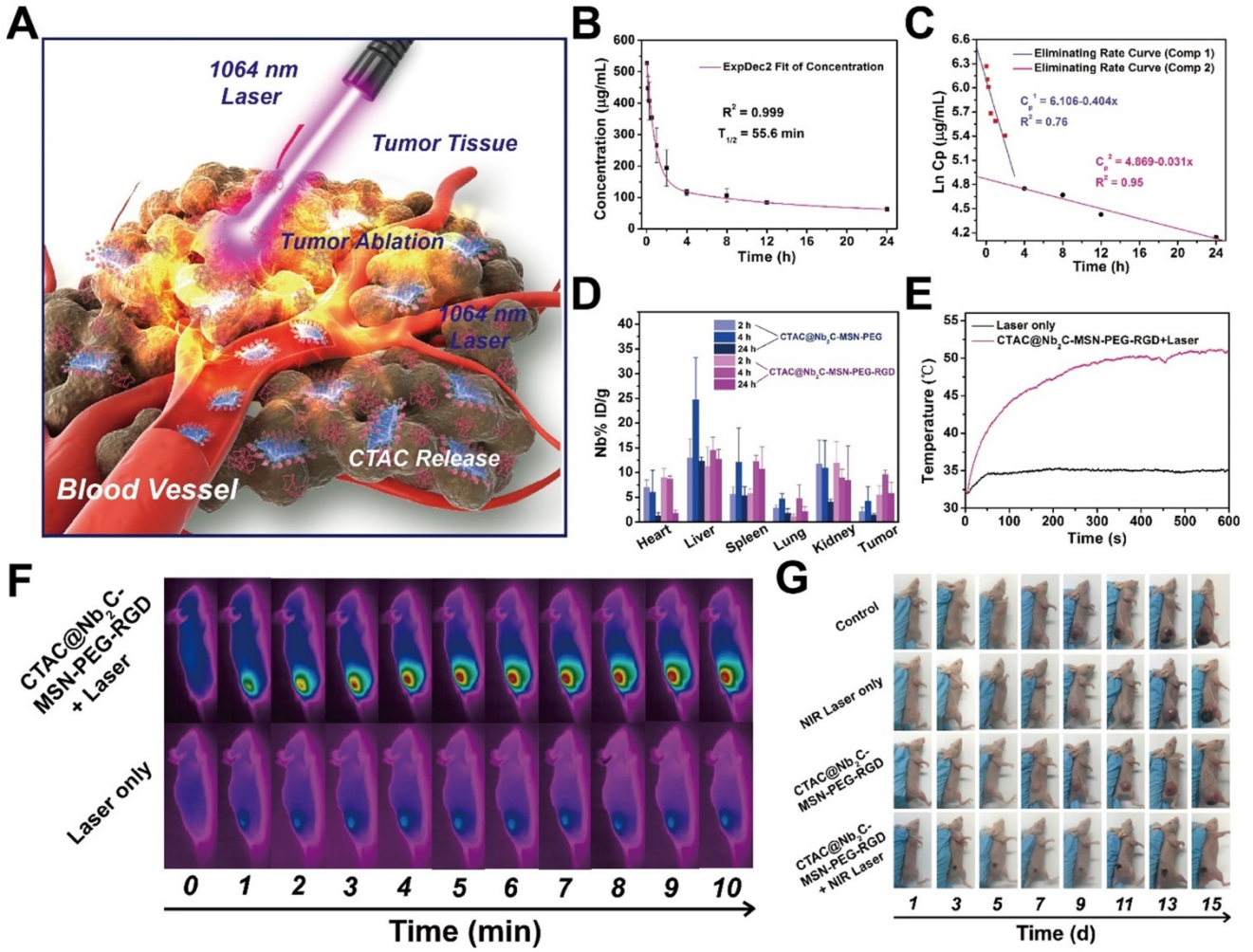

Figure 8. ***In vivo*** **pharmacokinetic analysis, biodistribution and photothermal effect. (A)** The scheme of *in vivo* enhanced chemotherapy and PTT as assisted by CTAC@Nb_2C-MSN-PEG-RGD for tumor treatment. **(B)** The blood circulation curve (ExpDec 2 means double exponential decay) of Si element concentration after intravenous injection of CTAC@Nb_2C-MSN-PEG-RGD and **(C)** the corresponding elimination rate curve calculated from the blood circulation curve (comp means component). **(D)** The biodistribution of Nb (%ID of Nb per g of tissues) in main organs and tumor tissue after intravenous injection of CTAC@Nb_2C-MSN-PEG-RGD for 2 h, 4 h and 24 h. **(E)** Temperature elevation of the tumor in U87 tumor-bearing mice under 1064 nm laser irradiation at a laser intensity of 1.5 W/cm² for 600 s with or without intravenous administration of CTAC@Nb_2C-MSN-PEG-RGD, and **(F)** corresponding IR images of U87 tumor-bearing mice under irradiation at varied time intervals (0, 1, 2, 3, 4, 5, 6, 7, 8, 9 and 10 min). **(G)** Digital photographs of mice for 15 days after the different treatments.

9A). In addition, hematoxylin and eosin (H&E) staining of major organs (heart, liver, spleen, lung and kidney) from U87-bearing nude mice 1 d and 15 d after various treatments also exhibited no obvious pathological changes (**Figure S11** and **Figure S12**), indicating high therapeutic biosafety. Importantly, the tumor-bearing mice in the group of CTAC@Nb_2C-MSN-PEG-RGD combined with laser irradiation in the NIR-II biowindow (1064 nm) exhibited significantly enhanced tumor-suppression effect with the tumors almost completely eradicated after the enhanced treatment (**Figure 9B-D**). The tumor inhibition efficiency reached 92.37% (**Figure 9E-F**), much higher than that of the CTAC@Nb_2C-MSN-PEG-RGD chemotherapeutic group (35.96%). Combined with pharmacokinetic analysis, biodistribution results and targeting assessment, this high therapeutic efficiency is attributed to the efficient accumulation of CTAC@Nb_2C-MSN-PEG-RGD composite nanosheets into the tumor tissue and further enhanced chemotherapy (by loaded CTAC) and photothermal hyperthermia (by Nb_2C MXene core).

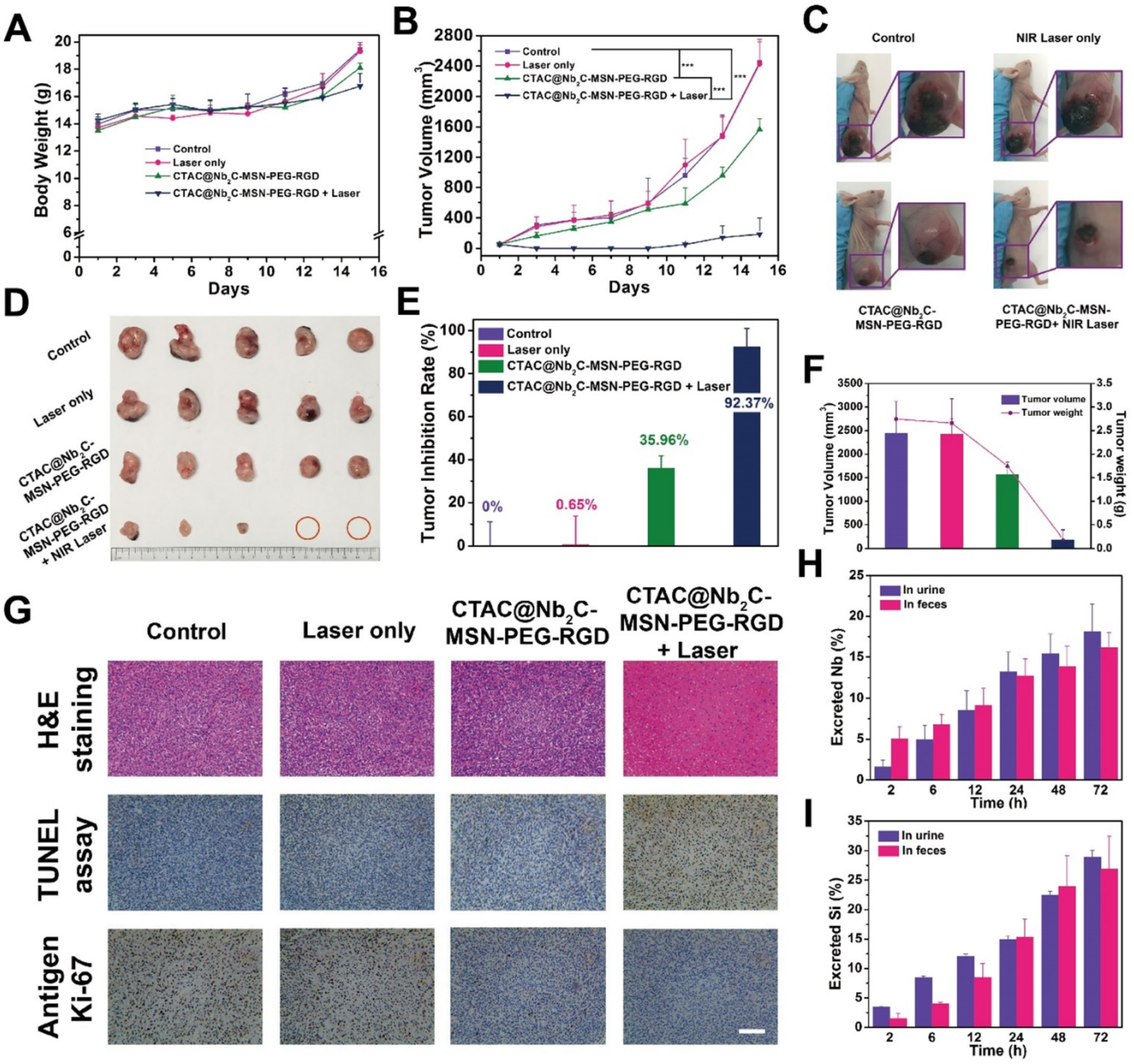

Figure 9. ***In vivo*** **enhanced chemotherapy/PTT. (A)** Time-dependent body-weight curves and **(B)** tumor-volume curves of U87 tumor-bearing mice in different groups (control group, CTAC@Nb_2C-MSN-PEG-RGD only group, laser only group, CTAC@Nb_2C-MSN-PEG-RGD combined with laser group). **(C)** Digital photos of U87 tumor-bearing mice and their tumor regions after varied treatments at day 15 post treatment, and **(D)** isolated tumor tissue after different treatments. **(E)** Tumor-inhibition rate and **(F)** the tumor volumes/weights of isolated tumors from each group at day 15 post treatment. **(G)** H&E staining, TUNEL staining and Antigen Ki-67 immunofluorescence staining in the tumor region of each group at day 15 post treatment. Scale bar: 50 μm. Accumulated **(H)** Nb excretion and **(I)** Si excretion after intravenous injection of CTAC@Nb_2C-MSN-PEG-RGD at different time points (2, 6, 12, 24, 48, and 72 h).

To determine the cell apoptosis of enhanced chemo/photothermal therapy by CTAC@Nb_2C-MSN-PEG-RGD combined with NIR-II laser irradiation, H&E, TdT-mediated dUTP nick-end labeling (TUNEL) and Antigen Ki-67 antibody were used to stain the tumor tissues. H&E and TUNEL images (**Figure 9G** and **Figure S13**) show that the group with highest efficacy for killing U87 cancer cells was CTAC@Nb_2C-MSN-PEG-RGD combined with 1064 nm laser irradiation as compared to the groups of control, laser only and CTAC@Nb_2C-MSN-PEG-RGD only. The proliferative status of the cancer cells was evaluated by Ki-67 antibody staining (**Figure 9G**), and the results also match the H&E and TUNEL results, suggesting high enhanced therapeutic efficacy based on CTAC@Nb_2C-MSN-PEG-RGD as chemo-therapeutic and photothermal conversion agent. Finally, the possible excretion pattern of these CTAC@Nb_2C-MSN-PEG-RGD composite nanosheets was preliminarily assessed. Both Nb (**Figure 9H**) and Si (**Figure 9I**) elements were found in the feces and urine, indicating that these composite nanosheets could gradually excrete out of the body *via* feces and urine, which is expected to avoid the accumulation risk of these nanoplatforms after their therapeutic purpose and further guaranteeing high therapeutic biosafety.

Conclusions

In summary, we have successfully constructed a "therapeutic mesopore" layer onto the surface of 2D Nb_2C MXene, which not only favors the surface engineering of 2D MXenes but also enhances their photothermal therapy by supplementary chemotherapy. In contrast to traditional chemodrug loading into mesopores, this work innovatively keeps the *in situ* self-assembled mesopore-making agent CTAC within the mesopores for chemotherapy, which avoids the tedious steps of surfactant extraction and chemodrug loading, and simultaneously guarantees high drug-loading capacity (32.57%). In particularly, such a "therapeutic mesopore" coating makes surface engineering possible, and efficient surface-targeting modification was achieved by RGD conjugation for selective recognition of integrin $\alpha_v\beta_3$ overexpressed on the cancer cell membrane. The unique photo-responsiveness of the 2D Nb_2C core in the composite nanosheets was demonstrated to exhibit high photothermal conversion capability (η: 28.6%) upon external laser irradiation in the NIR-II biowindow (1064 nm). Systematic *in vitro* and *in vivo* assessments demonstrated enhanced therapeutic efficacy of the "theranostic mesopore"-coated 2D Nb_2C against U87 brain cancer cells, not only at the intracellular level but also against subcutaneous tumor xenografts in nude mice (inhibition efficiency: 92.37%). The high therapeutic biosafety and easy excretion of these composite nanosheets was also revealed. This work not only provides an efficient strategy for surface engineering of 2D MXenes for satisfying versatile application requirements, but also significantly broadens the biomedical applications of 2D Nb_2C MXene for enhanced cancer therapy (PTT and chemotherapy in this case).

Abbreviations

2D: two-dimensional; APTES: (3-aminopropyl) triethoxysilane; CT: computed tomography; CTAC: Cetanecyltrimethylammonium chloride; c(RGDyC): cyclic arginine-glycine-aspartic pentapeptide; DAPI: 4',6-diamidino-2-phenylindole; DLS: dynamic light scattering; DMEM: Dulbecco's Modified Eagle Medium; EDS: energy dispersive spectrum mapping; EELS: electron energy loss spectroscopy; EPR: enhanced permeability and retention; FBS: fetal bovine serum; FITC: flurescein isothiocyanate; HCl: hydrochloric acid; HRTEM: High-resolution TEM image; H&E: hematoxylin and eosin; ICP-OES: inductively coupled plasma-optical emission spectrometry; Nb_2C: niobium carbide; NIR: near infrared; NPs: nanoparticles; PA: photoacoustic; PBS: phosphate buffer saline; PDT: photodynamic therapy; PI: propidium iodide; PTT: photothermal therapy; SBF: simulated body fluid; SD: standard deviation; SEM: scanning electron microscopy; TEA: triethanolamine; TEM: transmission electron microscopy; TEOS: tetraethylorthosilicate; TPAOH: tetrapropylammonium hydroxide; TUNEL: terminal deoxynucleotidyl transferase dUTP nick-end labeling; XPS: X-ray photoelectron spectroscopy; XRD: X-ray diffraction.

Supplementary Material

Supplementary methods and figures.
http://www.thno.org/v08p4491s1.pdf

Acknowledgements

We greatly acknowledge financial support from the National Key R&D Program of China (Grant No. 2016YFA0203700), National Natural Science Foundation of China (Grant No. 51722211, 51672303, 81760317, 31630026, 81771847 and 81630047) and Young Elite Scientist Sponsorship Program by CAST (Grant No. 2015QNRC001).

Competing Interests

The authors have declared that no competing interest exists.

References

1. Chen Y, Tan C, Zhang H, Wang L. Two-dimensional graphene analogues for biomedical applications. Chem Soc Rev. 2015; 44: 2681-701.
2. Yang K, Feng LZ, Shi XZ, Liu Z. Nano-graphene in biomedicine: theranostic applications. Chem Soc Rev. 2013; 42: 530-47.
3. Chen Y, Wang L, Shi J. Two-dimensional non-carbonaceous materials-enabled efficient photothermal cancer therapy. Nano Today. 2016; 11: 292-308.
4. Shao J, Xie H, Huang H, Li Z, Sun Z, Xu Y, et al. Biodegradable black phosphorus-based nanospheres for *in vivo* photothermal cancer therapy. Nat Commun. 2016; 7: 12967.
5. Ashley CE, Carnes EC, Phillips GK, Padilla D, Durfee PN, Brown PA, et al. The targeted delivery of multicomponent cargos to cancer cells by nanoporous particle-supported lipid bilayers. Nat Mater. 2011; 10: 389-97.
6. Yavuz MS, Cheng YY, Chen JY, Cobley CM, Zhang Q, Rycenga M, et al. Gold nanocages covered by smart polymers for controlled release with near-infrared light. Nat Mater. 2009; 8: 935-9.
7. Mi P, Kokuryo D, Cabral H, Wu H, Terada Y, Saga T, et al. A pH-activatable nanoparticle with signal-amplification capabilities for non-invasive imaging of tumour malignancy. Nat Nanotechnol. 2016; 11: 724.
8. Mikhaylov G, Mikac U, Magaeva AA, Itin VI, Naiden EP, Psakhye I, et al. Ferri-liposomes as an MRI-visible drug-delivery system for targeting tumours and their microenvironment. Nat Nanotechnol. 2011; 6: 594-602.
9. Ferrari M. Cancer nanotechnology: opportunities and challenges. Nat Rev Cancer. 2005; 5: 161-71.
10. Michalet X, Pinaud FF, Bentolila LA, Tsay JM, Doose S, Li JJ, et al. Quantum dots for live cells, *in vivo* imaging, and diagnostics. Science. 2005; 307: 538-44.
11. Dai C, Zhang S, Liu Z, Wu R, Chen Y. Two-dimensional graphene augments nanosonosensitized sonocatalytic tumor eradication. ACS Nano. 2017; 11: 9467-80.
12. Chen Y, Ye D, Wu M, Chen H, Zhang L, Shi J, et al. Break-up of two-dimensional MnO_2 nanosheets promotes ultrasensitive pH-triggered theranostics of cancer. Adv Mater. 2014; 26: 7019.
13. Feng LY, Wu L, Qu XG. New horizons for diagnostics and therapeutic applications of graphene and graphene Oxide. Adv Mater. 2013; 25: 168-86.
14. Cheng L, Liu J, Gu X, Gong H, Shi X, Liu T, et al. PEGylated WS_2 nanosheets as a multifunctional theranostic agent for *in vivo* dual-modal CT/photoacoustic imaging guided photothermal therapy. Adv Mater. 2014; 26: 1886-93.
15. Chimene D, Alge DL, Gaharwar AK. Two-dimensional nanomaterials for biomedical applications: emerging trends and future prospects. Adv Mater. 2015; 27: 7261.
16. Yang G, Gong H, Liu T, Sun X, Cheng L, Liu Z. Two-dimensional magnetic WS_2@Fe_3O_4 nanocomposite with mesoporous silica coating for drug delivery and imaging-guided therapy of cancer. Biomaterials. 2015; 60: 62-71.
17. Yang K, Zhang SA, Zhang GX, Sun XM, Lee ST, Liu ZA. Graphene in mice: ultrahigh *in vivo* tumor uptake and efficient photothermal therapy. Nano Lett. 2010; 10: 3318-23.
18. Liu Z, Robinson JT, Sun XM, Dai HJ. PEGylated nanographene oxide for delivery of water-insoluble cancer drugs. J Am Chem Soc. 2008; 130: 10876.
19. Chou SS, Kaehr B, Kim J, Foley BM, De M, Hopkins PE, et al. Chemically exfoliated MoS_2 as near-infrared photothermal agents. Angew Chem Int Edit. 2013; 52: 4160-4.
20. Sun Z, Xie H, Tang S, Yu XF, Guo Z, Shao J, et al. Ultrasmall black phosphorus quantum dots: synthesis and use as photothermal agents. Angew Chem Int Edit. 2015; 127: 11688-92.
21. Wang H, Yang X, Shao W, Chen S, Xie J, Zhang X, et al. Ultrathin black phosphorus nanosheets for efficient singlet oxygen generation. J Am Chem Soc. 2015; 137: 11376-82.
22. Liu T, Wang C, Gu X, Gong H, Cheng L, Shi X, et al. Drug delivery with PEGylated MoS_2 nano-sheets for combined photothermal and chemotherapy of cancer. Adv Mater. 2014; 26: 3433-40.
23. Chen W, Ouyang J, Liu H, Chen M, Zeng K, Sheng J, et al. Black phosphorus nanosheet-based drug delivery system for synergistic photodynamic/photothermal/chemotherapy of cancer. Adv Mater. 2016; 29: 1603864.
24. Lee HU, Park SY, Lee SC, Choi S, Seo S, Kim H, et al. Black phosphorus (BP) nanodots for potential biomedical applications. Small. 2016; 12: 214-9.
25. Naguib M, Mochalin VN, Barsoum MW, Gogotsi Y. 25th Anniversary Article: MXenes: a new family of two-dimensional materials. Adv Mater. 2014; 26: 992-1005.
26. Xu B, Zhu M, Zhang W, Zhen X, Pei Z, Xue Q, et al. Ultrathin MXene-micropattern-based field-effect transistor for probing neural activity. Adv Mater. 2016; 28: 3333-9.
27. Wang X, Kajiyama S, Iinuma H, Hosono E, Oro S, Moriguchi I, et al. Pseudocapacitance of MXene nanosheets for high-power sodium-ion hybrid capacitors. Nat Commun. 2015; 6: 6544.
28. Lukatskaya MR, Mashtalir O, Ren CE, Dall'Agnese Y, Rozier P, Taberna PL, et al. Cation intercalation and high volumetric capacitance of two-dimensional titanium carbide. Science. 2013; 341: 1502-5.
29. Ling Z, Ren CE, Zhao M-Q, Yang J, Giammarco JM, Qiu J, et al. Flexible and conductive MXene films and nanocomposites with high capacitance. Proc Natl Acad Sci USA. 2014; 111: 16676-81.
30. Naguib M, Kurtoglu M, Presser V, Lu J, Niu J, Heon M, et al. Two-dimensional nanocrystals produced by exfoliation of Ti_3AlC_2. Adv Mater. 2011; 23: 4248-53.
31. Naguib M, Gogotsi Y. Synthesis of two-dimensional materials by selective extraction. Acc Chem Res. 2015; 48: 128-35.
32. Ghidiu M, Lukatskaya MR, Zhao M-Q, Gogotsi Y, Barsoum MW. Conductive two-dimensional titanium carbide 'clay' with high volumetric capacitance. Nature. 2014; 516: 78-U171.
33. Naguib M, Mashtalir O, Carle J, Presser V, Lu J, Hultman L, et al. Two-dimensional transition metal carbides. ACS Nano. 2012; 6: 1322-31.
34. Rasool K, Helal M, Ali A, Ren CE, Gogotsi Y, Mahmoud KA. Antibacterial activity of $Ti_3C_2T_x$ MXene. ACS Nano. 2016; 10: 3674-84.
35. Dai C, Chen Y, Jing X, Xiang L, Yang D, Lin H, et al. Two-dimensional tantalum carbide (MXenes) composite nanosheets for multiple imaging-guided photothermal tumor ablation. ACS Nano. 2017; 11: 12696-712.
36. Lin H, Wang X, Yu L, Chen Y, Shi J. Two-dimensional ultrathin MXene ceramic nanosheets for photothermal conversion. Nano Lett. 2017; 17: 384-91.
37. Lin H, Gao S, Dai C, Chen Y, Shi J. A Two-dimensional biodegradable niobium carbide (MXene) for photothermal tumor eradication in NIR-I and NIR-II biowindows. J Am Chem Soc. 2017; 139: 16235-47.
38. Xuan J, Wang Z, Chen Y, Liang D, Cheng L, Yang X, et al. Organic-base-driven intercalation and delamination for the production of functionalized titanium carbide nanosheets with superior photothermal therapeutic performance. Angew Chem Int Edit. 2016; 55: 14569-74.
39. Liu G, Zou J, Tang Q, Yang X, Zhang Y, Zhang Q, et al. Surface modified Ti_3C_2 MXene nanosheets for tumor targeting photothermal/photodynamic/chemo synergistic therapy. ACS Appl Mater Interfaces. 2017; 9: 40077-86.
40. Lin H, Wang Y, Gao S, Chen Y, Shi J. Theranostic 2D tantalum carbide (MXene). Adv Mater. 2018; 30.
41. Hong GS, Lee JC, Robinson JT, Raaz U, Xie LM, Huang NF, et al. Multifunctional *in vivo* vascular imaging using near-infrared II fluorescence. Nat Med. 2012; 18: 1841.
42. Jiang Y, Li J, Zhen X, Xie C, Pu K. Dual-peak absorbing semiconducting copolymer nanoparticles for first and second near-infrared window photothermal therapy: a comparative study. Adv Mater. 2018; 30: 1705980.
43. Chen Y, Chen HR, Shi JL. Construction of homogenous/heterogeneous hollow mesoporous silica nanostructures by silica-etching chemistry: principles, synthesis, and applications. Acc Chem Res. 2014; 47: 125-37.
44. Trewyn BG, Slowing II, Giri S, Chen H-T, Lin VSY. Synthesis and functionalization of a mesoporous silica nanoparticle based on the sol-gel process and applications in controlled release. Acc Chem Res. 2017; 40: 846-53.
45. Chen Y, Chen H, Guo L, He Q, Chen F, Zhou J, et al. Hollow/rattle-type mesoporous nanostructures by a structural difference-based selective etching strategy. ACS Nano. 2009; 4: 529-39.
46. Chen Y, Chen HR, Zeng DP, Tian YB, Chen F, Feng JW, et al. Core/shell structured hollow mesoporous nanocapsules: a potential platform for simultaneous cell imaging and anticancer drug delivery. ACS Nano. 2010; 4: 6001-13.
47. Zhao WR, Chen HR, Li YS, Li L, Lang MD, Shi JL. Uniform rattle-type hollow magnetic mesoporous spheres as drug delivery carriers and their sustained-release property. Adv Funct Mater. 2008; 18: 2780-8.
48. Chen Y, Chen HR, Shi JL. *In vivo* bio-safety evaluations and diagnostic/therapeutic applications of chemically designed mesoporous silica nanoparticles. Adv Mater. 2013; 25: 3144-76.
49. Chen Y, Shi J. Chemistry of mesoporous organosilica in nanotechnology: molecularly organic–inorganic hybridization into frameworks. Adv Mater. 2016; 28: 3235-72.
50. Kim T, Momin E, Choi J, Yuan K, Zaidi H, Kim J, et al. Mesoporous silica-coated hollow manganese oxide nanoparticles as positive T(1) contrast agents for labeling and MRI tracking of adipose-derived mesenchyrnal stem cells. J Am Chem Soc. 2011; 133: 2955-61.
51. Lee JE, Lee N, Kim H, Kim J, Choi SH, Kim JH, et al. Uniform mesoporous dye-doped silica nanoparticles decorated with multiple magnetite nanocrystals for simultaneous enhanced magnetic resonance imaging, fluorescence imaging, and drug delivery. J Am Chem Soc. 2010; 132: 552-7.
52. Wang Y, Wang K, Zhao J, Liu X, Bu J, Yan X, et al. Multifunctional mesoporous silica-coated graphene nanosheet used for chemo-photothermal synergistic targeted therapy of glioma. J Am Chem Soc. 2013; 135: 4799-804.
53. Wang Y, Huang R, Liang G, Zhang Z, Zhang P, Yu S, et al. MRI-visualized, dual-targeting, combined tumor therapy using magnetic graphene-based mesoporous silica. Small. 2014; 10: 109-16.
54. Hope MA, Forse AC, Griffith KJ, Lukatskaya MR, Ghidiu M, Gogotsi Y, et al. NMR reveals the surface functionalisation of Ti_3C_2 MXene. Phys Chem Chem Phys. 2016; 18: 5099-102.
55. Ambrogio MW, Thomas CR, Zhao YL, Zink JI, Stoddartt JF. Mechanized silica nanoparticles: a new frontier in theranostic nanomedicine. Acc Chem Res. 2011; 44: 903-13.
56. Mamaeva V, Sahlgren C, Linden M. Mesoporous silica nanoparticles in medicine-recent advances. Adv Drug Deliv Rev. 2013; 65: 689-702.
57. Vallet-Regi M, Balas F, Arcos D. Mesoporous materials for drug delivery. Angew Chem Int Edit. 2007; 46: 7548-58.
58. Slowing, II, Vivero-Escoto JL, Wu CW, Lin VSY. Mesoporous silica nanoparticles as controlled release drug delivery and gene transfection carriers. Adv Drug Deliv Rev. 2008; 60: 1278-88.
59. Li ZX, Barnes JC, Bosoy A, Stoddart JF, Zink JI. Mesoporous silica nanoparticles in biomedical applications. Chem Soc Rev. 2012; 41: 2590-605.

60. He QJ, Gao Y, Zhang LX, Zhang ZW, Gao F, Ji XF, et al. A pH-responsive mesoporous silica nanoparticles-based multi-drug delivery system for overcoming multi-drug resistance. Biomaterials. 2011; 32: 7711-20.
61. He QJ, Shi JL, Chen F, Zhu M, Zhang LX. An anticancer drug delivery system based on surfactant-templated mesoporous silica nanoparticles. Biomaterials. 2010; 31: 3335-46.
62. Robinson JT, Tabakman SM, Liang YY, Wang HL, Casalongue HS, Vinh D, et al. Ultrasmall reduced graphene oxide with high near-infrared absorbance for photothermal therapy. J Am Chem Soc. 2011; 133: 6825-31.
63. Zeng J, Goldfeld D, Xia Y. A plasmon-assisted optofluidic (PAOF) system for measuring the photothermal conversion efficiencies of gold nanostructures and controlling an electrical switch. Angew Chem Int Edit. 2013; 52: 4169-73.
64. Hessel CM, Pattani VP, Rasch M, Panthani MG, Koo B, Tunnell JW, et al. Copper selenide nanocrystals for photothermal therapy. Nano Lett. 2011; 11: 2560-6.
65. Chen X, Paul KU, Zhen X, Manojit P, Pu K. Self-quenched semiconducting polymer nanoparticles for amplified *in vivo* photoacoustic imaging. Biomaterials. 2017; 119: 1–8.
66. Jiang Y, Pu K. Advanced photoacoustic imaging applications of near-infrared absorbing organic nanoparticles. Small. 2017; 13: 1700710.
67. Zhang J, Zhen X, Paul KU, Chen P, Pu K, et al. Activatable photoacoustic nanoprobes for *in vivo* ratiometric imaging of peroxynitrite. Adv Mater. 2017; 29: 1604764.
68. Jiang Y, Paul KU, Xie C, Yan L, Pu K, et al. Broadband absorbing semiconducting polymer nanoparticles for photoacoustic imaging in second near-infrared window. Nano Lett. 2017; 17: 4964–4969.
69. Jiang Y, Pu K. Molecular fluorescence and photoacoustic imaging in the second near-infrared optical window using organic contrast agents. Adv Biosyst. 2018; 2: 1700262.